

Phase transformation dynamics guided alloy design for additive manufacturing

Qilin Guo^{1,2}, Minglei Qu^{1,2}, Chihpin Andrew Chuang³, Lianghua Xiong⁴, Ali Naba^{1,2}, Zachary A. Young^{1,4}, Yang Ren³, Peter Kenesei³, Fan Zhang^{5,*}, Lianyi Chen^{1,2,**}

¹Department of Mechanical Engineering, University of Wisconsin–Madison, Madison, Wisconsin 53706, USA

²Department of Materials Science and Engineering, University of Wisconsin–Madison, Madison, Wisconsin 53706, USA

³X-ray Science Division, Argonne National Laboratory, Lemont, Illinois 60439, USA

⁴Department of Mechanical and Aerospace Engineering, Missouri University of Science and Technology, Rolla, Missouri 65409, USA

⁵Materials Measurement Science Division, National Institute of Standards and Technology, Gaithersburg, Maryland 20899, USA

** Corresponding author: lianyi.chen@wisc.edu

* Co-corresponding author: fan.zhang@nist.gov

Abstract

Fusion-based additive manufacturing technologies can make geometrically and compositionally complex parts unachievable by conventional manufacturing methods. However, the non-uniform and far-from-equilibrium heating/cooling conditions pose great challenge to obtaining consistent desirable phases in the as-printed parts. Here we report phase transformation dynamics guided design of precipitation hardening stainless steel with consistent formation of desired fully martensite structure across a wide range of cooling rates (10^2 – 10^7 °C/s). The phase transformation dynamics during laser melting was revealed by in-situ high-speed high-energy high-resolution X-ray diffraction. The designed alloy exhibits a tensile strength of 1364 MPa in the as-printed condition, which is comparable to the wrought counterpart after precipitation hardening heat treatment. The superior as-printed property is attributed to the fully martensite structure and the fine precipitates formed during printing. The phase transformation dynamics guided alloy design strategy demonstrated here opens the path for development of reliable high-performance alloys specific for AM.

Introduction

Fusion-based additive manufacturing (AM), e.g., laser powder bed fusion, directed energy deposition, integrates material synthesis and part manufacturing into a single step, which has the potential to revolutionize the manufacturing industry by enabling customized production of geometrically and compositionally complex parts with unprecedented functionality and performance^{1,2}.

However, the complex thermal conditions, intrinsic to the localized heat source-material interaction, pose big challenges to obtaining consistent desired phases in the as-printed parts, especially for materials with multi-stage phase transformation during solidification (e.g., steel³, titanium alloy⁴, nickel superalloy^{5,6}). First, the rapid cooling makes the solidification occur far from equilibrium, which may cause the phase transformation sequence/timing to deviate from the equilibrium phase diagram^{7,8}. Second, the heating/cooling conditions at different locations of the melt pool are different, which may lead to diversified phase constitutions within a single melt pool^{9,10}. Third, the thermal conditions across different machines, across different parts within a batch, and even across different regions within a single part are all different, which leads to inconsistent phase constitutions from print to print¹¹.

One prominent case is 17-4 precipitation hardening (PH) martensitic stainless steel (also known as 17-4 PH or type 630 stainless steel), which exhibits various unwanted phases in the as-printed condition¹². In conventional manufacturing with low cooling rate, 17-4 PH steel solidifies following liquid (L)– δ -ferrite (δ)–austenite (γ)–martensite (α') sequence according to the equilibrium phase diagram¹³. The desired final phase in 17-4 PH steel is martensitic phase (α'), which endows the material with excellent mechanical performance. However, in additively manufactured 17-4 parts, the as-printed phase is not fully martensite, but always contains residual δ phase and/or γ phase, whose fractions vary significantly across different printing parameters, machines, and AM technologies^{14–23}. The existence of residual δ phase and/or γ phase deteriorates the properties of the printed parts and the variation of the phase fraction causes significant quality uncertainty^{18,22,24–26}.

Here we report the design of 17-4 precipitation hardening martensitic stainless steel with formation of fully martensitic phase across a wide range of cooling rates (10^2 – 10^7 °C/s), guided by the phase transformation dynamics revealed by in-situ high-speed high-energy high-resolution synchrotron x-ray diffraction. The phase transformation dynamics results guided our design to focus on the liquid-solid phase transformation during initial solidification, which is different from the previous efforts/strategy that mainly focuses on the solid-solid phase transformation. The great tolerance to cooling rate variation of the designed alloy enables us to achieve fully martensitic phase in the as-printed condition with superior properties.

Results

In-situ characterization of phase transformation dynamics

We used in-situ laser-melting X-ray diffraction (XRD) experiment to probe the phase transformation dynamics in 17-4 PH stainless steel, as schematically illustrated in Fig. 1a. A fiber laser with a D4 σ diameter of ~ 100 μm was used to scan and melt the material to create a localized melt pool. Laser scan speed was varied from 0.05 m/s to 0.4 m/s to realize different cooling rates. During laser scanning, a stationary micro-focused high-energy high-flux monochromatic

synchrotron X-ray (1-ID of Argonne National Laboratory’s Advanced Photon Source (APS)) with a wavelength of 0.202153 Å and a beam size of 50 μm (H) × 30 μm (V) was transmitted through the sample (0.5 mm thick) to form Debye-Scherrer diffraction cones, which were projected into diffraction rings on a flat plate detector with a recording frame rate of 250 Hz. The diffraction rings from each frame were radially integrated along the whole azimuth range (0°–360°) to obtain intensity versus Q -vector patterns.

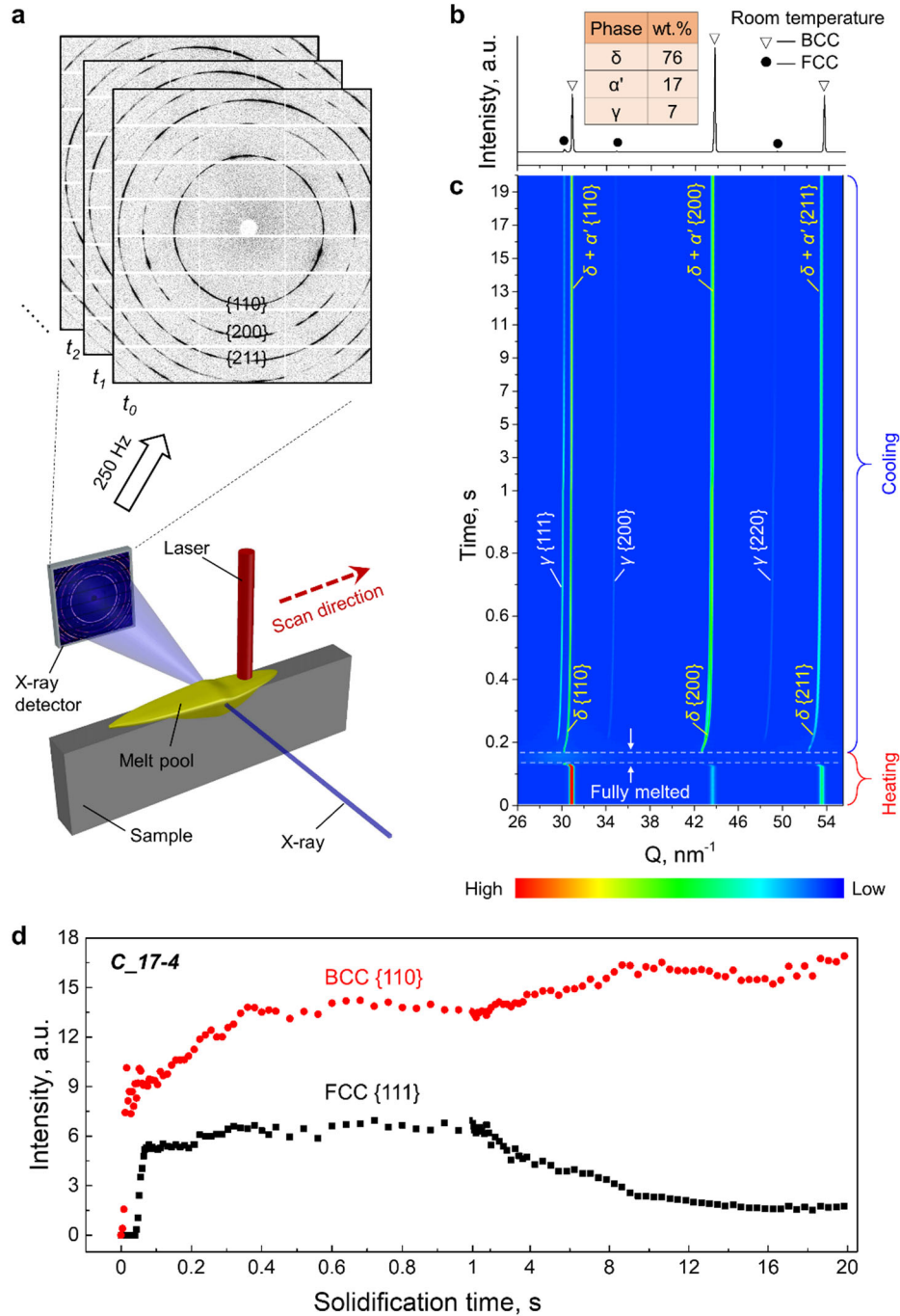


Fig. 1 | *In-situ characterization of phase transformation dynamics during laser melting. a, Schematic illustration of in-situ laser-melting X-ray diffraction experiment. A vertical laser beam*

scans the sample to create a localized melt pool. The micro-focused high-energy X-ray beam is used to probe the phase transformation dynamics with a frame rate of 250 Hz. **b**, Room temperature XRD pattern of as-solidified commercial additively manufactured 17-4 stainless steel (C_17-4) after laser melting. **c**, XRD intensity map (XRD peak intensity evolution as a function of time) during laser melting of C_17-4 from 0 s to 20 s. The liquid gap without any peaks denotes the time period when all the material in X-ray path is fully melted. The time axis is enlarged in the 0-1 s range to show the phase transformation details during laser melting. **d**, XRD intensity evolution from **c** during solidification. The time axis is enlarged in the 0-1 s range.

An example of the integrated XRD pattern is shown in Fig. 1b, exhibiting the room-temperature phase constitution of commercial AMed 17-4 PH stainless steel (hereinafter, C_17-4) after laser melting. As illustrated in Fig. 1b, the high brilliance and high energy (short wavelength) of the synchrotron X-ray ensured a good diffraction quality with high signal-to-noise ratio and wide Q -space range (covering more families of crystallographic planes), such that quantitative analysis could be carried out from the diffraction patterns. The high penetration of synchrotron X-ray into the metals provided bulk information of the specimen, which ruled out the potential surface effect (deformation-induced γ - α' transformation) caused by sample preparation¹⁴.

To visualize the phase transformation dynamics in C_17-4 during laser melting, the integrated XRD patterns were organized as a function of time to form an XRD intensity map, as shown in Fig. 1c. The time axis is enlarged at 0 s–1 s region to highlight the details during laser melting. The evolution of XRD intensities can be separated into two stages: a heating stage when the moving laser was approaching to the X-ray-illuminated area and then melting the material on the X-ray path, connected by a cooling stage when the laser moved away while the material started to solidify and cool down. During solidification, as indicated by Fig. 1c, δ -ferrite (δ) phase first came out from the liquid, followed by the formation of austenite (γ). In conventional manufacturing with slow cooling rate, a complete phase transformation of δ - γ and then γ - α' was expected, resulting in a martensite (α')-dominating final structure. However, during laser melting of C_17-4, neither of these two transformations was completed, as indicated by the continuous δ peaks in the intensity map (Fig. 1c) and the presence of FCC (face-centered cubic) peaks in the room-temperature XRD (Fig. 1b). (The lattice structure of austenite is FCC, while δ -ferrite and martensite have BCC (body-centered cubic) lattice structure in 17-4 PH steel.) The final phase constitution of C_17-4 after laser melting was estimated by Rietveld refinement analysis, indicating 76 wt.% residual δ -ferrite, 7 wt.% residual austenite, with only 17 wt.% desired martensite. (See **Method** for detailed phase fraction analysis.) For the first time, we directly demonstrated the existence of substantial amount of δ -ferrite in the as-printed 17-4 PH steel.

The cooling rate in our laser-melting experiment during initial solidification was estimated based on lattice parameter change. We measured the lattice parameter (a)–temperature (T) relationship by in-situ furnace heating/cooling XRD experiment performed at beamline 11-ID of APS. The sample was heated/cooled in a Linkam TS1500 Heating Stage with a rate of 20 °C/min within a temperature range of 50–1100 °C. A synchrotron X-ray beam with an energy of 105.7 keV reached the sample through the transparent window of the heating stage to generate XRD patterns, which were collected with a temperature increment of 50 °C. The lattice parameter a was calculated from Q -value of peak $\{hkl\}$ by $a = |Q|^{-1} \cdot 2\pi \cdot (h^2+k^2+l^2)^{0.5}$. The a - T relationship during heating and cooling of C_17-4 was established and shown in Fig. 2a, b. An intensity-versus-temperature curve

was obtained (Fig. 2c) to mark the phase transformation events during the process. The temperature was calibrated using Thermomechanical Analysis (TMA) on *C_17-4* (Fig. 2d) by assigning the martensite start temperature (M_s) and BCC–FCC transition temperature measured from TMA test (Fig. 2d) to the corresponding events denoted by X-ray intensity evolutions from in-situ testing (Fig. 2c). With the calibrated a – T relationship, we estimated the cooling rate during initial solidification of *C_17-4* in Fig. 1c to be 1.7×10^4 °C/s, by evaluating the lattice parameter change within a certain period (da/dt).

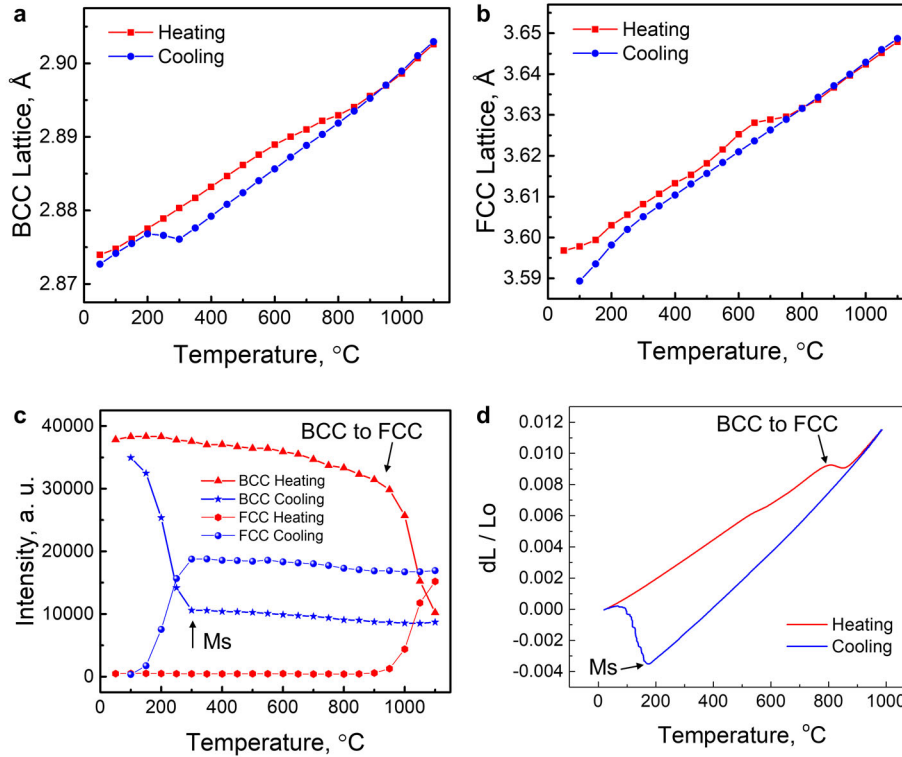


Fig. 2| Estimation of cooling rate. *a*, BCC lattice parameter change measured by in-situ furnace heating-cooling XRD test. *b*, FCC lattice parameter change during in-situ furnace heating-cooling XRD test. *c*, BCC and FCC diffraction peak intensity change as a function of temperature. *d*, Thermomechanical analysis (TMA) test showing the dilation as a function of temperature. The material is *C-17-4* and the heating/cooling rate is 20 °C/min for all tests.

Phase transformation dynamics guided alloy design based on phase fraction during initial solidification

Under the cooling rate of 1.7×10^4 °C/s, we observed a highly stabilized δ -ferrite, as indicated by the quantified XRD intensity evolution as a function of time in Fig. 1d. The BCC phase intensity keeps increasing during solidification, meaning the δ -ferrite in *C_17-4*—once formed—does not transform into austenite at all under the current cooling rate. It was previously reported that a very high cooling rate of 10^5 – 10^6 °C/s is needed to bypass the δ – γ transformation due to the insufficient time (up to ~ 6 ms) spent within the δ – γ transformation temperature range (roughly from 600–800 °C to 1250–1450 °C, depending on specific compositions)^{7,16,27,28}. However, our experiment was carried out under a lower cooling rate at the order of 10^4 °C/s, which extended the time in δ – γ transformation range by tenfold (at the order of ~ 60 ms), yet the δ – γ transformation still did not

happen, suggesting the initial solidified δ -ferrite was highly stabilized. Assuming (in the worst case scenario) no δ -ferrite transforms into austenite during rapid cooling, in order to get more desired martensite phase in the final 17-4 PH structure, the δ -ferrite amount at initial solidification must be reduced.

To minimize initial solidified δ -ferrite, we individually investigated the effect of three major alloying elements (Cr, Ni, Cu) on the maximum solidified δ -ferrite fraction using CALPHAD method. (See [Supplementary Fig. 1a, b](#) for details.) The results showed that, within 17-4 PH specification, a lower concentration of Cr with a higher concentration of Ni and Cu could reduce the maximum fraction of δ -ferrite at initial solidification. Additionally, more Cu can promote the formation of Cu-rich precipitates to enhance the strength of 17-4 PH steel. Thus, we designed our alloy with a composition of Fe_{74.7}Cr_{15.2}Ni_{4.8}Cu_{5.0}Nb_{0.3} (hereinafter named it *UW_17-4*), which has significantly reduced maximum δ -ferrite fraction ([Supplementary Fig. 1 c, d](#)). The chemical composition in as-cast *UW_17-4* was confirmed by inductively coupled plasma (ICP) analysis, with the result shown in [Table 1](#).

Table 1. Chemical composition (wt.%) of 17-4 PH stainless steel.

17-4 PH	Cr	Ni	Cu	Mn	Nb	C	N	O	Si	S	P	Fe
Specification	15.0-17.5	3.0-5.0	3.0-5.0	1.0 max.	0.15-0.45	0.07 max	–	–	1.0 max.	0.03 max.	0.04 max.	Bal.
C_17-4, ICP	16.7	4.3	4.0	0.22	0.3	0.02	0.027	0.058	0.34	0.003	0.011	Bal.
UW_17-4, ICP (Nominal)	15.29 (15.2)	4.78 (4.8)	4.91 (5.0)	<0.001 (–)	0.311 (0.3)	0.002 (–)	0.005 (–)	0.019 (–)	0.009 (–)	0.002 (–)	0.007 (–)	Bal.

Consistent phase formation under various cooling rates (tolerance to cooling rate variation)

To examine the phase transformation behavior of *UW_17-4* under rapid cooling condition, we carried out in-situ laser-melting XRD tests under various cooling rates from 1.7×10^4 °C/s to 8.1×10^4 °C/s. The complete phase transformation history under each condition were shown in X-ray intensity maps, [Fig. 3b, e, h](#), with the initial solidification enlarged at [Fig. 3c, f, i](#). During initial solidification, no δ -ferrite was observed to stay into austenite region, as indicated by the short-lived δ -ferrite peaks in [Fig. 3c, f](#), as well as the absence of δ -ferrite peak in [Fig. 3i](#). It suggests a reduced stability of δ -ferrite in *UW_17-4* as compared with that of *C_17-4*. As a consequence, the material swiftly became fully austenite structure from molten state. The austenite phase further transformed into martensite at a Ms temperature of 233 ± 21 °C, resulting in a fully BCC structure at the room temperature, as indicated by the XRD patterns in [Fig. 3a, d, g](#). Since no δ -ferrite survived from the initial solidification, the BCC signal solely came from martensite. Thus, fully martensitic structure was achieved in as-solidified *UW_17-4* under all of the three cooling rates.

The absence of initial-solidified δ -ferrite in [Fig. 3i](#) deviates from the CALPHAD calculation. It is possible that the recording frame rate in our in-situ experiment (250 Hz) was not enough to capture the δ -ferrite formation under high cooling rate (8.1×10^4 °C/s). Future research is needed to provide more conclusive evidence to facilitate fundamental understanding of transient solidification behavior during rapid cooling of 17-4 PH steel.

Since the feasible cooling rate window for in-situ observation is limited (by frame rate), we conducted ex-situ laser melting and casting experiments to further study the as-solidified microstructure in *UW_17-4* with extended range of cooling rates by electron backscatter

diffraction (EBSD), as displayed in Fig. 4. Three cooling rates in the order of 10^2 °C/s, 10^4 °C/s, and 10^7 °C/s were investigated in samples fabricated by casting (arc-melting), single-layer laser melting, and laser spot welding, respectively. To be noticed, the sample made under 10^4 °C/s is within the cooling rate window of the in-situ experiment to serve as a reference here.

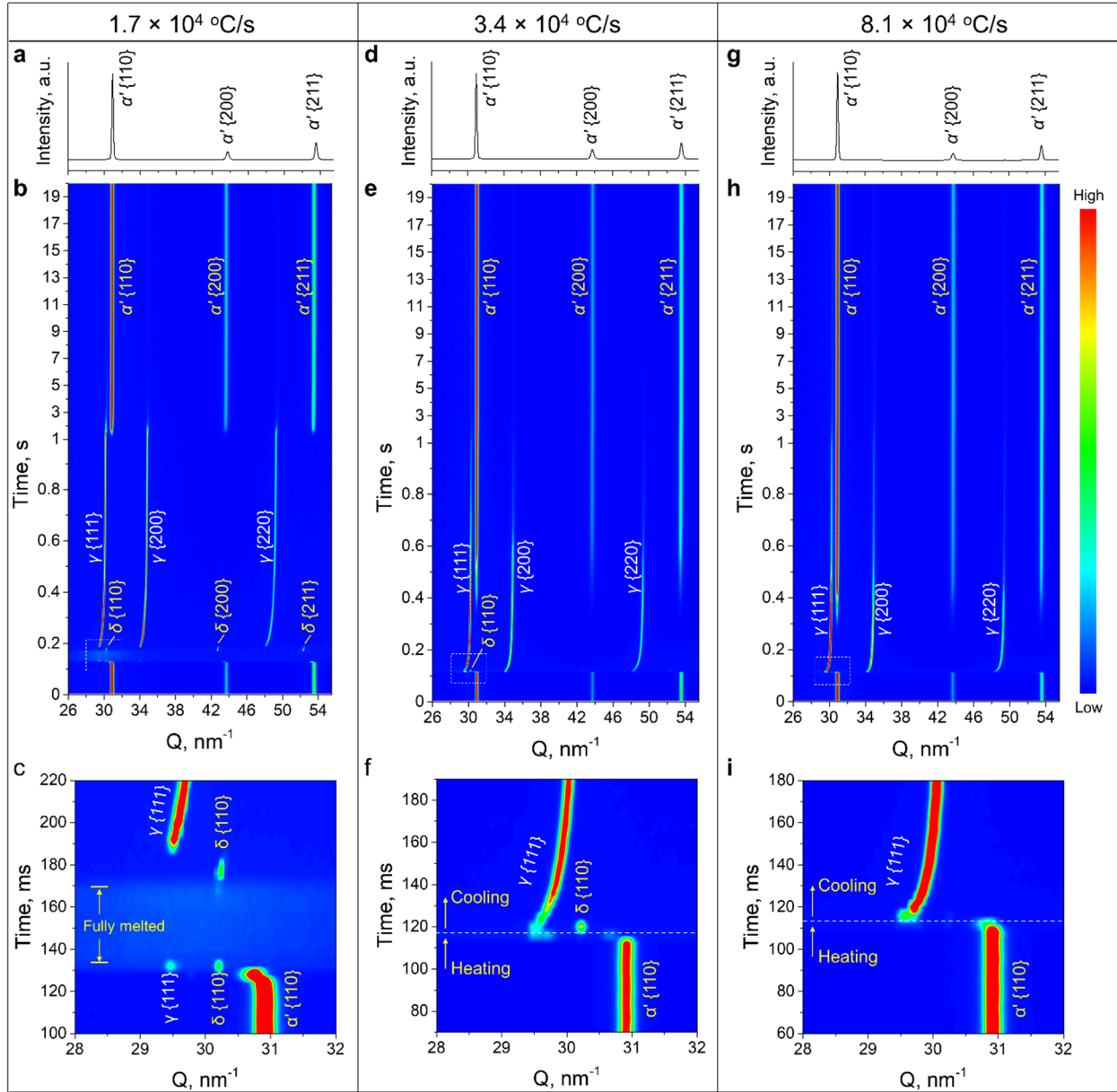


Fig. 3| Phase evolution of UW_17-4 under various cooling rates. *a*, Room temperature XRD of as-solidified UW_17-4 after laser melting with a cooling rate of 1.7×10^4 °C/s. *b*, XRD intensity map during laser melting from 0 s to 20 s with a cooling rate of 1.7×10^4 °C/s. *c*, Zoom-in view from *b* to highlight the phase transformation at initial solidification. *d-f*, XRD results under a cooling rate of 3.4×10^4 °C/s. *g-i*, XRD results under a cooling rate of 8.1×10^4 °C/s.

The microstructure under the three cooling rates (10^2 °C/s, 10^4 °C/s, 10^7 °C/s) were all identified to be fully martensitic, as indicated by the image quality (IQ) maps on the right panels in Fig. 4a-

c. The consistent dark netlike-features in three IQ maps are signatures of martensite resulting from its poor diffraction quality caused by the internal high-density lattice defects (such as dislocations and sub-grain boundaries)²⁸⁻³⁰. A slight difference in contrast is observed in the IQ map of Fig. 4b, where the left half field-of-view is darker than the right half. It is because a refined structure was obtained during rapid cooling, as exhibited in the inversed pole figure (IPF) of Fig. 4b.

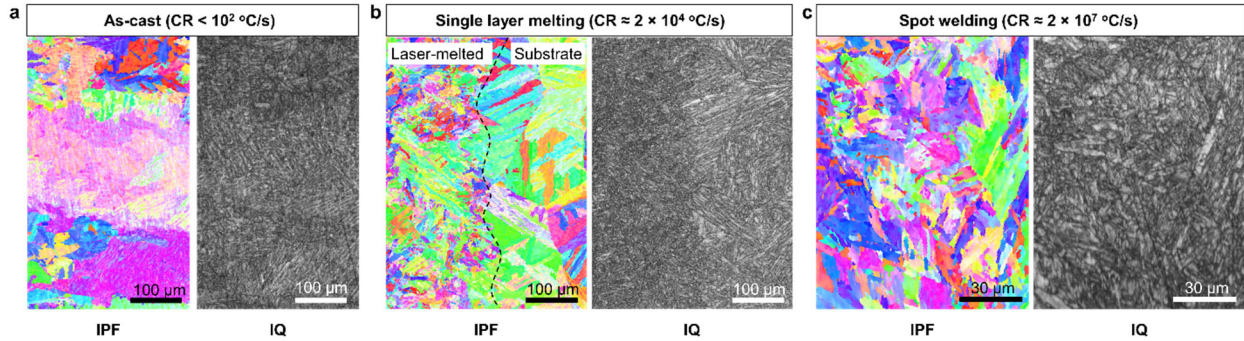


Fig. 4| Microstructure of as-solidified UW_17-4 under various cooling rates. a, EBSD of as-cast UW_17-4 fabricated by arc-melting. The left panel is inversed pole figure (IPF). The right panel is image quality (IQ) map. **b,** EBSD of UW_17-4 after a single-layer laser melting. The substrate is cast UW_17-4 after solution heat-treatment (fully martensite). **c,** EBSD of UW_17-4 after laser spot welding under 156 W with 1 ms laser duration. The microstructure for all conditions are fully martensitic.

Therefore, with in-situ and postmortem examination, we showed that our designed alloy, UW_17-4, can consistently produce fully martensitic final structure under a broad range of cooling rates ($10^2 - 10^7$ °C/s), which covers all types of fusion-based AM technologies.

Tolerance to environment impurity

In addition to the resistance to cooling rates, a robust material for AM must have good tolerance to environment impurities. Environment impurities in AM refer to the elements that are excluded or out of the range of the alloy specifications. It is almost inevitable to entrain environment impurities to the alloy during AM process.

Here, we demonstrate UW_17-4 can consistently produce fully martensitic structure with impurity in the processing environment. To simulate environment impurities, we mixed 20 vol.% air with the rest 80 vol.% shielding argon gas. In such environment, we re-melted the same location of the material for up to three times, monitored by the in-situ XRD system. The results are shown in Fig. 5. The final phase structure after the 3rd re-melting is still fully martensitic, as validated by the fully BCC peaks in Fig. 5g and the complete $\delta-\gamma-\alpha'$ transformation in Fig. 5h, i. In addition, across the three results, we did not observe significant difference in terms of phase transformation sequence and temperature, indicating a good tolerance of UW_17-4 to common environment impurities.

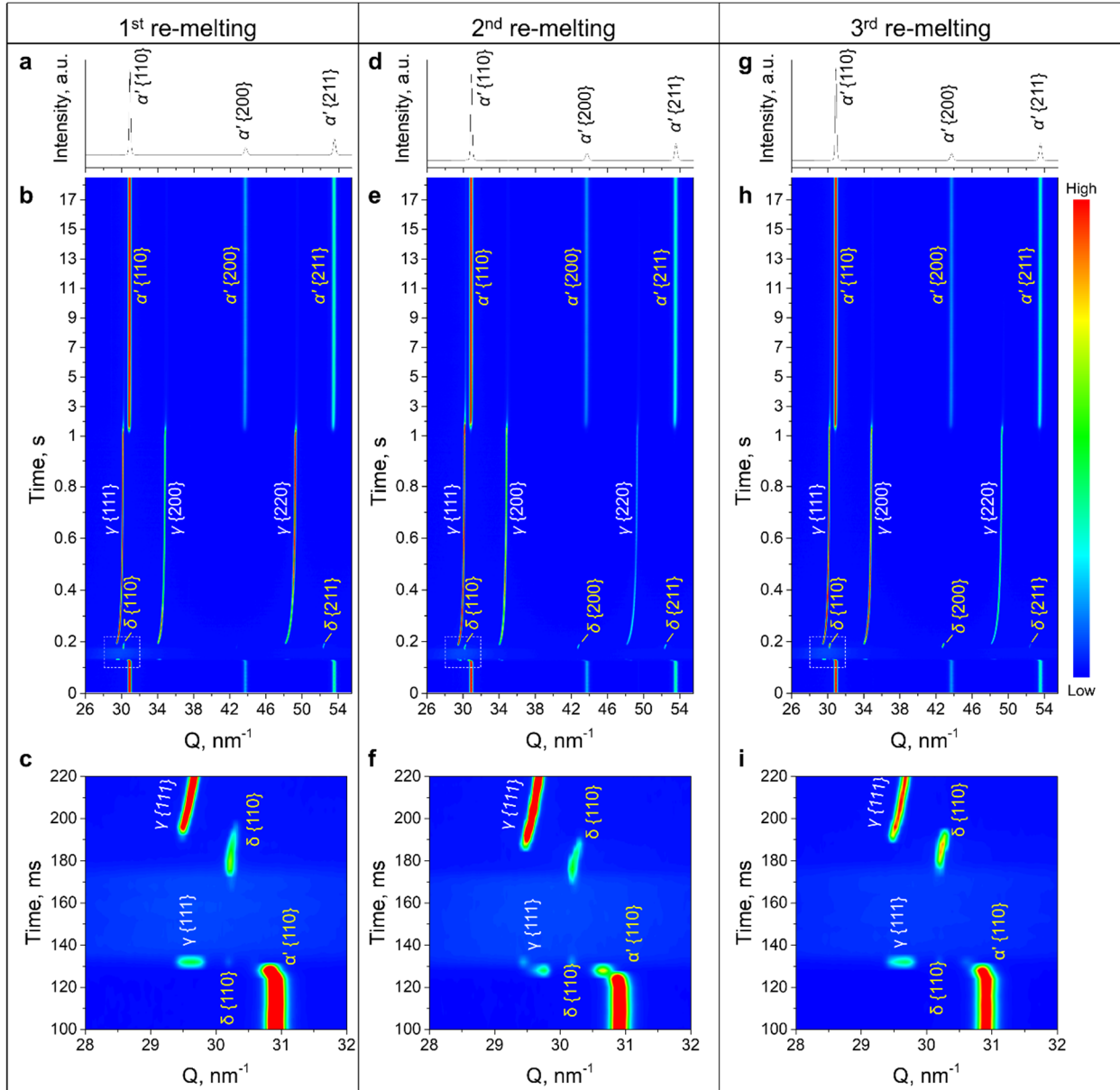


Fig. 5| Phase evolution of UW_17-4 with impurity in the environment gas. The processing environment contains 80 vol.% argon as main protection gas and 20 vol.% air as impurity. **a**, Room temperature XRD of as-solidified UW_17-4 after 1st laser re-melting. **b**, XRD intensity map during 1st laser re-melting from 0 s to 18.5 s. **c**, Zoom-in view from **b** to highlight phase transformation at initial solidification. **d-f**, XRD results of laser re-melting for the 2nd time at the same location as in **a-c**. **g-i**, XRD results of laser re-melting for the 3rd time at the same location as in **a-c**.

Structure and property of as-printed UW_17-4

To validate our designed alloy in real AM process, we fabricated a UW_17-4 part on our in-house laser powder-bed fusion system. The final structure in the as-printed part was tested to be nearly fully BCC structure (99.9 wt.%), as shown by the synchrotron XRD in Fig. 6a, which contains bulk information from a sampling volume of 1.0 mm × 0.6 mm × 0.8 mm. Further EBSD

examination revealed fully martensitic features on IQ map of as-printed *UW_17-4* (Fig. 6b), similarly to the ones shown in Fig. 4. Given the combined information from Fig. 6a, b, the as-printed *UW_17-4* part is fully martensitic.

Tensile testing was performed to characterize the mechanical properties of the samples. The ultimate tensile strength of the as-printed *UW_17-4* is compared with its counterparts, including as-printed *C_17-4*, wrought 17-4 after solution heat-treatment (fully martensitic), and wrought 17-4 after H900 heat-treatment (fully martensitic + precipitation hardening). The results summarized in Fig. 6d show that: (1) the as-printed *UW_17-4* exhibited an ultimate tensile strength (UTS) of 1364 ± 10.4 MPa, which is ~60% (506 MPa) higher than that of the as-printed *C_17-4*; (2) the UTS of the *UW_17-4* in the as-printed condition is comparable to that of the wrought 17-4 after precipitation hardening heat treatment.

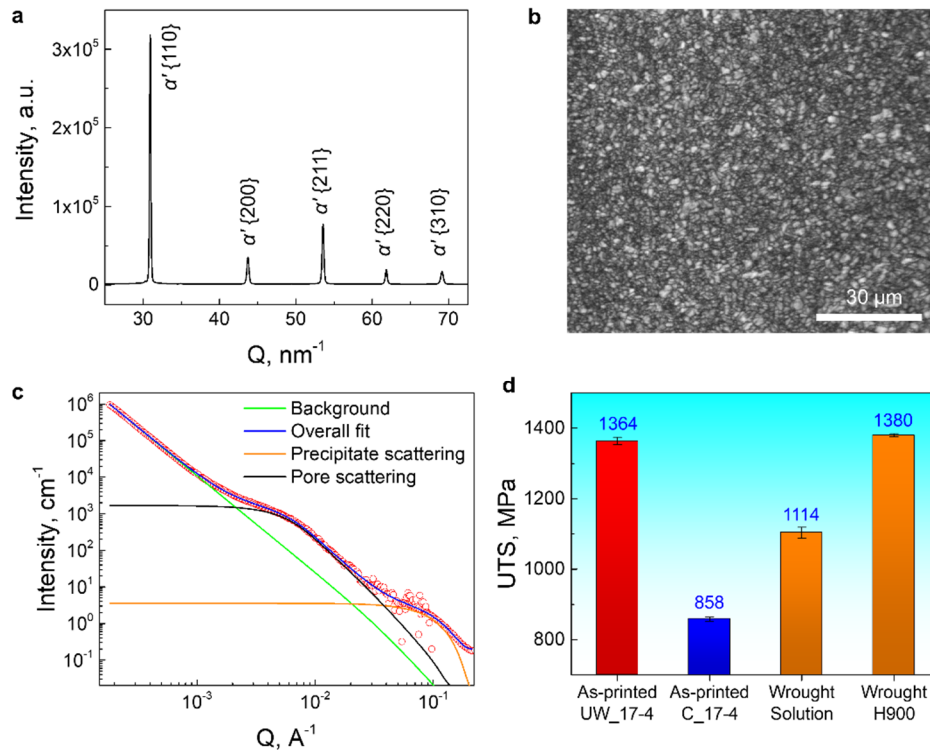


Fig. 6 | Structure and property of as-printed *UW_17-4*. *a*, High-resolution synchrotron XRD of as-printed *UW_17-4*. The sample volume along X-ray penetration was $1.0 \text{ mm} \times 0.6 \text{ mm} \times 0.8 \text{ mm}$. *b*, IQ map of as-printed *UW_17-4* by EBSD characterization. *c*, Small-angle X-ray scattering (SAXS) of as-printed *UW_17-4*. *d*, Ultimate tensile strength (UTS) of commercial wrought 17-4 PH steel after solution heat treatment (Wrought solution), commercial wrought 17-4 PH steel after H900 heat treatment (Wrought H900), as-printed *C_17-4*, and as-printed *UW_17-4*.

Being fully martensitic is not enough to explain the high UTS of the as-printed *UW_17-4* because otherwise it would have a similar UTS to the solution heat-treated wrought 17-4. A possible reason for the unexpected high UTS is the existence of copper-rich precipitates, which are a major contributor to the extra strength in precipitation hardened wrought 17-4²⁶. We performed small-angle X-ray scattering (SAXS) test on *UW_17-4* to check whether there are precipitations in the as-printed part. The SAXS test collected bulk information from a specimen of $5 \text{ mm} \times 5 \text{ mm} \times 100$

μm . The result is shown in Fig. 6c, where a characteristic length on the scale of 4 nm (orange line) was observed. This size fits the description of copper-rich precipitates^{32,33}. It is likely that they were formed during the cyclic heating/cooling process in AM, which is equivalent to an in-situ heat-treatment process. An additional characteristic length on the scale of 50 nm also showed up on the SAXS curve in Fig. 6c, which is attributed to the metallurgical pores in the material (as shown in Supplementary Fig. 2).

Summary

In summary, guided by phase transformation dynamics, we designed a robust martensitic stainless steel (*UW_17-4*) for additive manufacturing that can consistently produce fully martensitic structure in the as-solidified state under a wide range of cooling rates (10^2 – 10^7 °C/s) and withstand common environment impurities. The as-printed *UW_17-4* exhibits superior properties in the as-printed condition. The alloy design strategy reported here indicates the importance of understanding phase transformation dynamics under AM conditions. We expect that phase transformation dynamics guided alloy design will lead to design of robust high-performance materials for additive manufacturing industry.

Methods

Materials

The *C_17-4* for in-situ detection and tensile testing was fabricated by commercial laser powder-bed fusion machine with commercial feedstock powder (argon-atomized). The chemical composition is tested by inductively coupled plasma (ICP) analysis, as shown in Table 1. The samples are in as-printed state before tests without any post heat-treatment.

The *UW_17-4* for in-situ detection were cast in an arc melter (model SP-MSM20-8, MTI Corporation, USA) with pure elements pre-weighted by a balance (model PA224C, OHAUS Corporation, USA) with measuring accuracy of 0.0001 g. The purity of base elements is 99.98% for Fe, 99.995% for Cr, 99.995% for Ni, 99.995% for Cu, and 99.97% for Nb. The arc melting current was 185 amperes with melting time of 15–25 s until the material was fully melted. The ingot was flipped and re-melted for 6 times to ensure composition uniformity. The cast ingot went through a Condition-A solution heat treatment (heating rate 15 °C/min, holding at 1038 ± 5 °C for 45 min) in a KSL-1500 Muffle Furnace (MTI Corporation, USA) followed by water quenching. The final phase after quenching was fully martensite (confirmed by synchrotron XRD and EBSD).

The as-printed *UW_17-4* was made in our open architecture laser powder-bed fusion system. The feedstock powder was argon-atomized using as-cast ingots. The laser power was 520 W with 0.1 m/s scan speed. The nominal $D4\sigma$ beam size was 170 μm . The powder layer thickness was 50 μm .

The wrought 17-4 PH steel was supplied from McMaster-Carr in annealed state. Solution heat-treatment and then H900 heat-treatment (482 ± 5 °C, holding 1 hour) were performed to make samples for tensile testing.

In-situ laser melting synchrotron X-ray diffraction experiment

The in-situ XRD experiment was carried out on beamline 1-ID-C at the Advanced Photon Source (APS), Argonne National Laboratory (ANL), Chicago, USA. The setup was described in previously published papers ^{34,35}. The configuration of laser beam, X-ray beam, and the sample positioning is schematically shown in Fig. 1a. During the test, the sample was placed in a vacuum chamber refilled with argon for protection. A continuous-wave single-mode ytterbium fiber laser (model YLR-500-AC, IPG Photonics, USA) controlled by a galvo scanner (IntelliSCANde 30, SCANLAB GmbH, Germany) was used to perform laser scanning/melting on the samples. The maximum laser output power was 520 W with a wavelength of 1070 nm. The $1/e^2$ laser beam size was set to $\sim 100 \mu\text{m}$. The high-energy (61.293 keV) synchrotron X-ray radiated at the side of the sample, with a cross-sectional beam dimension of $30 \mu\text{m}$ (vertical) \times $50 \mu\text{m}$ (horizontal), where x-ray was vertically focused with FWHM of $30 \mu\text{m}$ and horizontal dimension was confined by slits. The scattered X-ray was collected by a PILATUS3X-2M CdTe X-ray detector (DECTRIS, Switzerland) with a frame rate of 250 Hz. The X-ray exposure time was 1 ms.

XRD peak analysis

The 360° diffraction rings were batch-processed by FIT2D software and converted into tables of scattering intensities versus Q -vector ($Q = 4\pi \cdot \sin(\theta)/\lambda$, with θ being one half of the scattering angle 2θ , and λ being the X-ray wavelength). Each integrated pattern included 2048 bins in a Q range of 26 nm^{-1} to 55.5 nm^{-1} . The peak position and peak intensity were determined by Gauss + Lorentz function.

Determination of phase fraction

Rietveld refinement was performed by GSAS-II software to determine the phase fraction from XRD patterns. The standard phase information was acquired from Inorganic Crystal Structure Database (ICSD) with IDs of ICSD-53449 (austenite), ICSD-53452 (delta-ferrite), and ICSD-53451 (alpha-ferrite). A standard CeO₂ powder specimen was used to calibrate the experiment configuration. The background, scale factor, lattice constants, grain size, and microstrain were all considered in the refinement. The determination of final phase constitution in as-printed C₁₇₋₄ (Fig. 1b) took two steps. We first determined the FCC and BCC phase fraction at a neutral temperature ($\sim 400 \text{ }^\circ\text{C}$) where the δ - γ transformation has finished, yet γ - α' has not started. Therefore, all the BCC phase at this moment will become residual δ -ferrite to room temperature. We then determined the FCC and BCC phase fraction at room temperature. The increased fraction of BCC phase as compared to neutral temperature must come from the α' phase resulting from γ - α' transformation.

Thermal analysis

In-situ furnace heating/cooling X-ray diffraction experiments were carried out at APS beamline 11-ID-C by heating up a sample in a Linkam TS1500 Heating Stage (Linkam Scientific Instruments) with heating/cooling rate of $20 \text{ }^\circ\text{C}/\text{min}$ within a temperature range of 50 – $1100 \text{ }^\circ\text{C}$. XRD patterns were acquired every $50 \text{ }^\circ\text{C}$. Lattice parameters above $1100 \text{ }^\circ\text{C}$ was obtained by linear extrapolation. Thermomechanical analysis (TMA) was performed on NETZSCH TMA 402 F1,

following ASTM E831-19 standard. The heating/cooling rate was 20 °C/min within a temperature range of 50–1000 °C. Both experiments were shielded by high purity argon (99.999%).

Tensile test

Tensile tests were performed on an MTS Criterion 40 electromechanical universal test system (Model 43). The strain rate was $2.5 \times 10^{-4} \text{ s}^{-1}$. The geometry and dimensions of the specimens follow the tensile specimen design (MT2) developed for additively manufactured metals reported in reference³⁷. All specimens were cut by wire electrical discharge machining (EDM) followed by surface grinding to 1200 grit (5 μm).

Small-angle X-ray scattering (SAXS) experiment

We performed small-angle X-ray scattering (SAXS) measurement at the ultra-small-angle X-ray scattering beamline 9-ID-C of the Advanced Photon Source, Argonne National Laboratory, to determine the nanoscopic microstructural features in the as-built 17-4 steel. Because of its Bonse-Hart crystal optics, this instrument provides primary intensity calibration, enabling analysis of absolute volume fraction of scattering inhomogeneities³⁸. We used a standard configuration of this instrument to acquire ultra-small-angle X-ray scattering, SAXS, and X-ray diffraction data of the same sample volume across a broad Q range from $1 \times 10^{-4} \text{ \AA}^{-1}$ to 6.5 \AA^{-1} .³⁸ A detailed description of this setup can be found in reference³⁹. The X-ray energy was 21 keV, corresponding to an X-ray wavelength of 0.5904 \AA . We carefully polished a thin foil of as-built 17-4 steel with a thickness of $\approx 100 \text{ \mu m}$ (transmission of $\approx 14 \%$) to ensure penetration. We analyzed the data using standard small angle scattering analysis software Irena⁴⁰.

Data availability

The data supporting the findings of this work is available in the main text or supplementary materials. Raw data are available from the corresponding authors on reasonable request.

References

- [1] T. DebRoy, T. Mukherjee, H.L. Wei, J.W. Elmer, J.O. Milewski, Metallurgy, mechanistic models and machine learning in metal printing, *Nat. Rev. Mater.* 6 (2021) 48–68.
- [2] T.D. Ngo, A. Kashani, G. Imbalzano, K.T.Q. Nguyen, D. Hui, Additive manufacturing (3D printing): A review of materials, methods, applications and challenges, *Compos. Part B Eng.* 143 (2018) 172–196.
- [3] H. Fayazfar, M. Salarian, A. Rogalsky, D. Sarker, P. Russo, V. Paserin, E. Toyserkani, A critical review of powder-based additive manufacturing of ferrous alloys: Process parameters, microstructure and mechanical properties, *Mater. Des.* 144 (2018) 98–128.
- [4] M. Qian, W. Xu, M. Brandt, H.P. Tang, Additive manufacturing and postprocessing of Ti-6Al-4V for superior mechanical properties, *MRS Bull.* 41 (2016) 775–784.

- [5] W.M. Tucho, P. Cuvillier, A. Sjolyst-Kverneland, V. Hansen, Microstructure and hardness studies of Inconel 718 manufactured by selective laser melting before and after solution heat treatment, *Mater. Sci. Eng. A.* 689 (2017) 220–232.
- [6] K. Amato, Comparison of Microstructures and Properties for a Ni-Base Superalloy (Alloy 625) Fabricated by Electron Beam Melting, *J. Mater. Sci. Res.* 1 (2012).
- [7] M. Alnajjar, F. Christien, C. Bosch, K. Wolski, A.D. Fortes, M. Telling, In-situ neutron diffraction study of wrought and selective laser melted maraging stainless steels, *Mater. Charact.* 172 (2021) 110840.
- [8] A.J. Shahani, A.J. Clarke, Processing metallic materials far from equilibrium, *MRS Bull.* 45 (2020) 906–909.
- [9] X. Tan, Y. Kok, Y.J. Tan, M. Descoins, D. Mangelinck, S.B. Tor, K.F. Leong, C.K. Chua, Graded microstructure and mechanical properties of additive manufactured Ti–6Al–4V via electron beam melting, *Acta Mater.* 97 (2015) 1–16.
- [10] P. Kürsteiner, M.B. Wilms, A. Weisheit, B. Gault, E.A. Jäggle, D. Raabe, High-strength Damascus steel by additive manufacturing, *Nature.* 582 (2020) 515–519.
- [11] Y. Kok, X.P. Tan, P. Wang, M.L.S. Nai, N.H. Loh, E. Liu, S.B. Tor, Anisotropy and heterogeneity of microstructure and mechanical properties in metal additive manufacturing: A critical review, *Mater. Des.* 139 (2018) 565–586.
- [12] L. Zai, C. Zhang, Y. Wang, W. Guo, D. Wellmann, X. Tong, Y. Tian, Laser powder bed fusion of precipitation-hardened martensitic stainless steels: A review, *Metals (Basel).* 10 (2020) 255.
- [13] C.N. Hsiao, C.S. Chiou, J.R. Yang, Aging reactions in a 17-4 PH stainless steel, *Mater. Chem. Phys.* 74 (2002) 134–142.
- [14] E.A. Lass, F. Zhang, C.E. Campbell, Nitrogen effects in additively manufactured martensitic stainless steels: conventional thermal processing and comparison with wrought, *Metall. Mater. Trans. A.* 51 (2020) 2318–2332.
- [15] A.A. Adeyemi, E. Akinlabi, R.M. Mahamood, K.O. Sanusi, S. Pityana, M. Tlotleng, Influence of laser power on microstructure of laser metal deposited 17-4 PH stainless steel, *IOP Conf. Ser. Mater. Sci. Eng.* 225 (2017) 012028.
- [16] M. Alnajjar, F. Christien, K. Wolski, C. Bosch, Evidence of austenite by-passing in a stainless steel obtained from laser melting additive manufacturing, *Addit. Manuf.* 25 (2019) 187–195.
- [17] L. Facchini, N. Vicente, I. Lonardelli, E. Magalini, P. Robotti, A. Molinari, Metastable austenite in 17-4 precipitation-hardening stainless steel produced by selective laser melting, *Adv. Eng. Mater.* 12 (2010) 184–188.
- [18] L.E. Murr, E. Martinez, J. Hernandez, S. Collins, K.N. Amato, S.M. Gaytan, P.W. Shindo, Microstructures and properties of 17-4 PH stainless steel fabricated by selective laser melting, *J. Mater. Res. Technol.* 1 (2012) 167–177.

- [19] P. Leo, M. Cabibbo, A. Del Prete, S. Giganto, S. Martínez-Pellitero, J. Barreiro, Laser defocusing effect on the microstructure and defects of 17-4PH parts additively manufactured by SLM at a low energy input, *Metals (Basel)*. 11 (2021) 588.
- [20] T.-H. Hsu, P.-C. Huang, M.-Y. Lee, K.-C. Chang, C.-C. Lee, M.-Y. Li, C.-P. Chen, K.-K. Jen, A.-C. Yeh, Effect of processing parameters on the fractions of martensite in 17-4 PH stainless steel fabricated by selective laser melting, *J. Alloys Compd.* 859 (2021) 157758.
- [21] I. Mathoho, E.T. Akinlabi, N. Arthur, M. Tlotleng, Impact of DED process parameters on the metallurgical characteristics of 17-4 PH SS deposited using DED, *CIRP J. Manuf. Sci. Technol.* 31 (2020) 450–458.
- [22] A. Caballero, J. Ding, S. Ganguly, S. Williams, Wire + Arc Additive Manufacture of 17-4 PH stainless steel: Effect of different processing conditions on microstructure, hardness, and tensile strength, *J. Mater. Process. Technol.* 268 (2019) 54–62.
- [23] F.S.H.B. Freeman, A. Lincoln, J. Sharp, A. Lambourne, I. Todd, Exploiting thermal strain to achieve an in-situ magnetically graded material, *Mater. Des.* 161 (2019) 14–21.
- [24] H.K. Rafi, D. Pal, N. Patil, T.L. Starr, B.E. Stucker, Microstructure and mechanical behavior of 17-4 precipitation hardenable steel processed by selective laser melting, *J. Mater. Eng. Perform.* 23 (2014) 4421–4428.
- [25] X. Wang, G. Wang, T. Shi, Y. Wang, Tensile mechanical behavior and spall response of a selective laser melted 17-4 PH stainless steel, *Metall. Mater. Trans. A.* 52 (2021) 2369–2388.
- [26] A. Yadollahi, N. Shamsaei, S.M. Thompson, A. Elwany, L. Bian, Effects of building orientation and heat treatment on fatigue behavior of selective laser melted 17-4 PH stainless steel, *Int. J. Fatigue.* 94 (2017) 218–235.
- [27] F. Villaret, X. Boulnat, P. Aubry, J. Zollinger, D. Fabrègue, Y. de Carlan, Modelling of delta ferrite to austenite phase transformation kinetics in martensitic steels: Application to rapid cooling in additive manufacturing, *SSRN Electron. J.* (2021) DOI: 10.2139/ssrn.3782879.
- [28] S. Vunnam, A. Saboo, C. Sudbrack, T.L. Starr, Effect of powder chemical composition on the as-built microstructure of 17-4 PH stainless steel processed by selective laser melting, *Addit. Manuf.* 30 (2019) 100876.
- [29] L. Ryde, Application of EBSD to analysis of microstructures in commercial steels, *Mater. Sci. Technol.* 22 (2006) 1297–1306.
- [30] J. Wu, P.J. Wray, C.I. Garcia, M. Hua, A.J. Deardo, Image quality analysis: A new method of characterizing microstructures, *ISIJ Int.* 45 (2005) 254–262.
- [31] S. Zaefferer, J. Ohlert, W. Bleck, A study of microstructure, transformation mechanisms and correlation between microstructure and mechanical properties of a low alloyed TRIP steel, *Acta Mater.* 52 (2004) 2765–2778.
- [32] G. Yeli, M.A. Auger, K. Wilford, G.D.W. Smith, P.A.J. Bagot, M.P. Moody, Sequential nucleation of phases in a 17-4PH steel: Microstructural characterisation and mechanical

- properties, *Acta Mater.* 125 (2017) 38–49.
- [33] Y. Sun, R.J. Hebert, M. Aindow, Effect of heat treatments on microstructural evolution of additively manufactured and wrought 17-4PH stainless steel, *Mater. Des.* 156 (2018) 429–440.
- [34] C. Zhao, K. Fezzaa, R.W. Cunningham, H. Wen, F. De Carlo, L. Chen, A.D. Rollett, T. Sun, Real-time monitoring of laser powder bed fusion process using high-speed X-ray imaging and diffraction, *Sci. Rep.* 7 (2017) 3602.
- [35] S.A. Oh, R.E. Lim, J.W. Aroh, A.C. Chuang, B.J. Gould, J. V. Bernier, N. Parab, T. Sun, R.M. Suter, A.D. Rollett, Microscale observation via high-speed X-ray diffraction of alloy 718 during in situ laser melting, *JOM.* 73 (2021) 212–222.
- [36] S. Karnati, I. Axelsen, F.F. Liou, J.W. Newkirk, Investigation of tensile properties of bulk and SLM fabricated 304L stainless steel using various gage length specimens, in: *Proc. 27th Annu. Int. Solid Free. Fabr. Symp. Addit. Manuf. Conf.*, 2016: pp. 592–604.
- [37] F. Zhang, J. Ilavsky, G.G. Long, J.P.G. Quintana, A.J. Allen, P.R. Jemian, Glassy carbon as an absolute intensity calibration standard for small-angle scattering, *Metall. Mater. Trans. A.* 41 (2010) 1151–1158.
- [38] J. Ilavsky, F. Zhang, R.N. Andrews, I. Kuzmenko, P.R. Jemian, L.E. Levine, A.J. Allen, Development of combined microstructure and structure characterization facility for in situ and operando studies at the Advanced Photon Source, *J. Appl. Crystallogr.* 51 (2018) 867–882.
- [39] F. Zhang, L.E. Levine, A.J. Allen, M.R. Stoudt, G. Lindwall, E.A. Lass, M.E. Williams, Y. Idell, C.E. Campbell, Effect of heat treatment on the microstructural evolution of a nickel-based superalloy additive-manufactured by laser powder bed fusion, *Acta Mater.* 152 (2018) 200–214.
- [40] J. Ilavsky, P.R. Jemian, Irena : tool suite for modeling and analysis of small-angle scattering, *J. Appl. Crystallogr.* 42 (2009) 347–353.

Acknowledgements

This work is funded by the National Science Foundation and University of Wisconsin-Madison Startup Fund. The authors acknowledge use of facilities and instrumentation at the UW-Madison Wisconsin Centers for Nanoscale Technology (wcnt.wisc.edu) partially supported by the NSF through the University of Wisconsin Materials Research Science and Engineering Center (DMR-1720415). This research used resources of the Advanced Photon Source, a U.S. Department of Energy (DOE) Office of Science User Facility operated for the DOE Office of Science by Argonne National laboratory under contract DE-AC02-06CH11357.

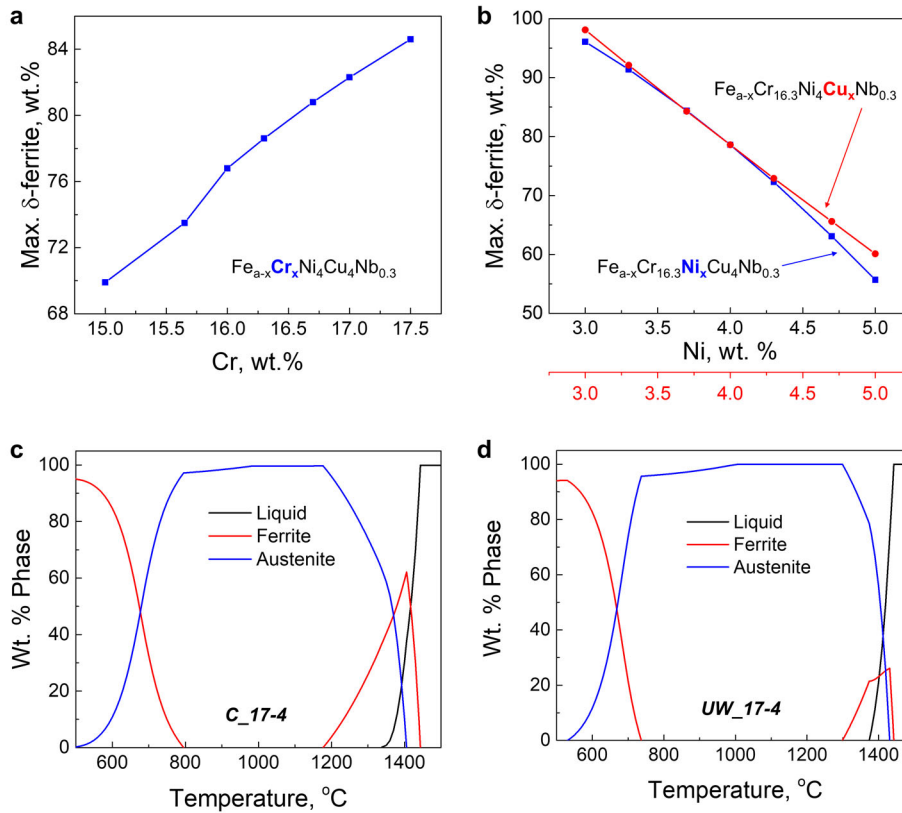
Author contributions

L.C. conceived the idea and supervised the research project. Q.G. and L.C. designed the alloys. Q.G., M.Q., C.C., L.X., Z.A.Y, and J.D.A. conducted the in-situ X-ray diffraction experiment. F.Z. supervised the SAXS experiment and analyzed the data. Q.G. and F.Z. did the CALPHAD calculation. Q.G. analyzed the data, conducted the mechanical test and microstructure analysis. F.Z., C.C., and L.C. supervised the methodology of X-ray data analysis. All authors discussed the results. Q.G., L.C. and F.Z. wrote the paper with input from all authors.

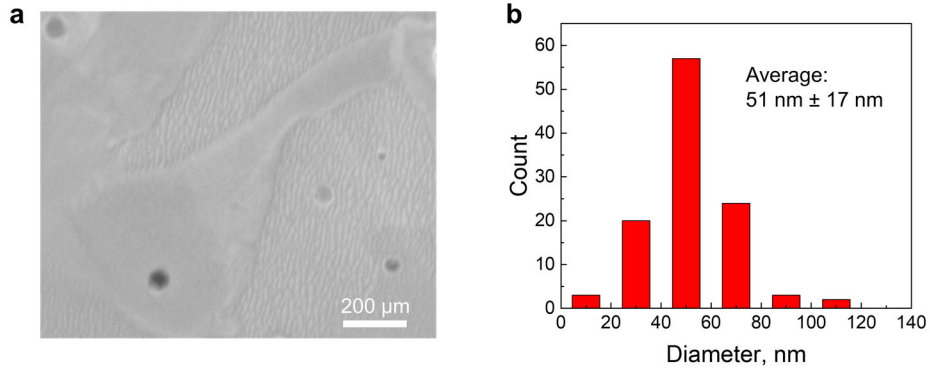
Conflict of interests

Wisconsin Alumni Research Foundation (WARF) has filed a patent with L.C. and Q.G. as inventors for the UW_17-4 alloy reported in this paper.

Supplementary Figures



Supplementary Fig. 1 | Phase fraction under equilibrium condition calculated using CALPHAD method. **a**, Maximum δ -ferrite weight fraction during solidification as a function of Cr concentration. Only major metallic elements (Fe, Cr, Ni, Cu, Nb) were included in the calculation. **b**, Maximum δ -ferrite weight fraction during solidification as a function of Ni and Cu concentration. **c**, Equilibrium phase transformation of C_17-4 during solidification. **d**, Equilibrium phase transformation of the designed 17-4 stainless steel (i.e. UW_17-4) during solidification.



Supplementary Fig. 2 | Metallurgical pores in as-printed UW_17-4. a, SEM image of the metallurgical pores. The sample surface was mechanically polished with 0.05 μm diamond suspension followed by ion milling. **b**, Statistics of the pores distributed within a 21.79 μm \times 14.55 μm area.